

Adaptive Control in Adaptive Optics for Directed Energy Systems *

Yu-Tai Liu and Steve Gibson
Mechanical and Aerospace Engineering
University of California
Los Angeles, CA 90095-1597
yutai@ucla.edu, gibson@ucla.edu

Abstract—This paper presents an adaptive control scheme for adaptive optics. Adaptive compensation is needed in many adaptive optics applications because wind velocities and the strength of atmospheric turbulence can change rapidly, rendering classical fixed-gain reconstruction algorithms far from optimal. The paper also presents a method for generating frequency-weighted deformable-mirror modes, which are important for optimal performance of the adaptive control scheme. The performance of the adaptive control scheme is illustrated by simulations of a directed energy system with a high energy laser propagating through extended turbulence.

I. INTRODUCTION

Adaptive optics (AO) refers to the use of deformable mirrors driven by active control loops that feedback wavefront sensor (WFS) measurements to compensate for turbulence-induced phase distortion of optical waves propagating through the atmosphere [1], [2], [3], [4], [5]. These control loops reconstruct (i.e., estimate and predict) the phase profile, or wavefront, from the WFS data. The control loops in classical AO systems are linear and time-invariant (LTI), having fixed gains based on assumed statistics of atmospheric turbulence. Such control loops are not themselves adaptive in the sense in which the term *adaptive* is used in the control and filtering literature, where *adaptive* normally refers to updating control and/or filter gains in real time.

Adaptive compensation is needed in many AO applications because wind velocities and the strength of atmospheric turbulence can change rapidly, rendering any fixed-gain reconstruction algorithm far from optimal. Recently, adaptive wavefront reconstruction algorithms based on recursive least-squares (RLS) estimation of optimal reconstructor matrices have been proposed [6], [7], [8], [9], [10], [11]. In this approach, an adaptive control loop augments a classical AO feedback loop. Results in [7], [8], [9] have shown that the type of adaptive loops used here are robust with respect to modeling errors and sensor noise.

The real-time computational burden is significant for adaptive wavefront reconstruction because the number of actuators and the number of sensors each can be on the order of 100 to 1000, while the digital control loops run at sample-and-hold rates of 1000 Hz and higher. It is a major challenge to develop real-time adaptive algorithms with RLS parameter estimation for a problem with so many input and output channels. For the adaptive control loops proposed here and in [7]–[11], a multichannel RLS lattice filter first presented in [12] has been

reparameterized and embedded in algorithms developed for adaptive disturbance rejection in adaptive optics problems. This multichannel lattice filter preserves the efficiency and numerical stability of simpler lattice filters, while performing channel-orthogonalization to accommodate large numbers of channels. Although the problem formulation and much of the structure of the adaptive control loop presented here do not require that a lattice filter be used for adaptive estimation of an optimal wavefront reconstructor, multichannel lattice filters are among the few classes of algorithms that can yield the speed and numerical stability required for real-time adaptive optics.

This paper presents several advances beyond previous publications on the use of adaptive filtering and control in adaptive optics. Here, the adaptive control loop operates on a set of tilt-removed deformable-mirror modes; a parallel track loop corrects the tilt on the laser beam. The input to the adaptive control loop here is the closed-loop wavefront sensor vector, as opposed to an estimate of the open-loop wavefront sensor vector, which was used in [7]–[9]. Following the descriptions of the adaptive optics problem and the adaptive control loops in Sections II and III, an alternative fixed-gain implementation is described in Section IV. This quasi-adaptive implementation has a much lower computational burden than the fully adaptive controller, and simulations show that it performs nearly as well as the adaptive controller when the turbulence statistics are stationary over periods of sufficient length. The frequency-weighted deformable-mirror modes introduced in Section V are significantly better for adaptive optics than the modes used in [7]–[11] because of the spatial filtering properties of the new modes and the relative ease of computing them. A high-fidelity wave optics propagation model of a high energy laser system is used here, so that the adaptive optics simulations presented in Section VI are much more realistic than those in [7]–[10]. This application is more challenging than those in [7]–[10] because the turbulence path is much longer.

A feature common to this paper and the methods in [6], [7], [8], [9], [10], [11] is that the adaptive control loop augments a classical AO loop. Section VII describes how the performance of the adaptive control loop and the performance the classical AO loop vary with the loop gain of the classical loop. This study also shows how modeling errors associated with the loop gain of the classical loop affect the performance of the adaptive control loop.

* This research was supported by AFOSR Grant F49620-02-1-0319.

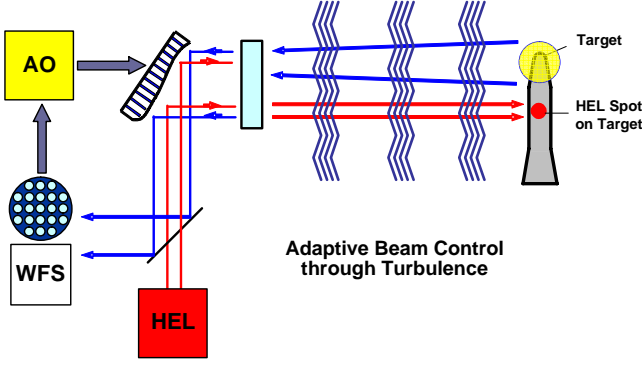


Fig. 1. Diagram of a directed energy system with high energy laser (HEL). Key components of the beam control system: adaptive optics algorithm (AO), deformable mirror (DM), wavefront sensor (WFS).

II. THE ADAPTIVE OPTICS PROBLEM

Figure 1 shows a schematic diagram for an adaptive optics problem in a directed energy weapon system. Actuators are distributed in a two-dimensional array over a deformable mirror. These actuators are driven to adjust the profile of the mirror surface and cancel the phase distortions induced in the high-energy laser beam as it propagates through atmospheric turbulence. A wave front sensor (WFS) measures the residual wavefront error, using an array of subapertures that sense the spatial derivatives, or slopes, of the phase profile on a grid interlaced with the locations of the actuators. The purpose of AO system is to compensate the outgoing high energy laser for the wavefront error that will be induced by atmospheric turbulence, so that the laser forms a fixed, tight spot (image) on the target. The control system uses a beacon created by illuminating the target with a low energy laser as the basis for determining the commands to the deformable mirror required to cancel turbulence-induced phase distortion. Because the beacon is considered to be a distant point source, the wavefront propagating from the beacon would be very nearly a plane wave when it reached the mirror with no atmospheric turbulence. This plane wave is the desired set point for the control algorithm. If the wavefronts propagating from the beacon to the target travel through approximately the same atmosphere, then correcting the wavefront from the beacon should compensate for the turbulence effects on outgoing beam.

For control design and simulation, the adaptive optics problem is represented by the block diagram in Figure 2. The measured wavefront slope vector is denoted by y , and the command vector to the deformable mirror (DM) is denoted by c . The objective of the control loops is to minimize the RMS value, over space and time, of the projection of y onto a certain subspace.

The block labeled WOP (wave optics propagation) Model in Figure 2 is a high-fidelity simulation of a directed energy problem like that represented in Figure 1. This model includes the propagation of both the beacon and high energy laser beams,

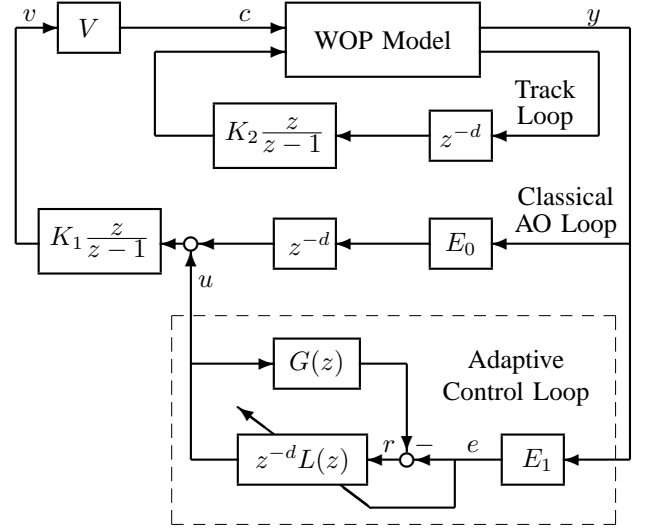


Fig. 2. Block diagram of the digital control loops for adaptive optics. Wave optics propagation (WOP) block includes turbulence, wavefront sensor, deformable mirror, and sensor and fast steering mirror for track loop.

as well as models of the wavefront sensor, deformable mirror, track loop, and focal plane imaging on both the adaptive optics platform and the target. For the research reported here, the wave optics model is the program WaveTrain [13]. The model used in this research is based on non-sensitive features of HEL systems.

For design of the control loops, it is assumed that WFS vector and DM command vector are related by

$$y = w - \Gamma c, \quad (1)$$

where Γ is the poke matrix and w is the wavefront error produced by atmospheric turbulence. In the WaveTrain model used for simulations in this paper, as in real AO systems, the relationship between the WFS vector and DM command vector is actually nonlinear, but the linear approximation in (1) has proved adequate for control system design. The linear model in (1) is used to design most classical AO systems, and it is important to note that the adaptive control loop presented here performs well even though its design assumes (1).

The top two feedback loops in Figure 2 are classical AO and track loops, with integrator gains K_1 and K_2 , respectively. These feedback loops are linear time-invariant (LTI) control loops. The blocks in Figure 2 labeled z^{-d} represent total loop latency, usually due to computation and sensor read-out delays. In most applications, the loop latency is $d = 1$ or $d = 2$.

The matrix V in the AO loop defines a parameterization of actuator space. The columns of V represent DM modes that are commanded independently by the control loops. Thus,

$$c = Vv \quad (2)$$

where the vector v contains the independent control commands generated by the AO loops. Such parameterizations have been used in [8], [9], [10], but the new method for computing

frequency weighted DM modes in Section V of this paper produces more desirable DM modes. As discussed in Section V, tilt was removed from the modes used for this paper, so that the AO and track loops are uncoupled—at least to the extent that the linear model in (1) is valid.

The reconstructor matrix E_0 in the classical AO loop is chosen to satisfy

$$E_0 \Gamma V = I. \quad (3)$$

Under this hypothesis and that in (1), the control channels represented by the components of the vector v are uncoupled; i.e., the control command represented by a single element of v affects only the error signal represented by the corresponding element of the error vector

$$\varepsilon = E_0 y, \quad (4)$$

which is the input to the integrator in the classical AO loop.

For the simulations reported in this paper, E_0 is equal to the pseudo inverse of ΓV . In this case, the objective of the classical AO loop is to cancel the orthogonal projection of the WFS vector y onto the range of ΓV , which is the image in sensor space of the subspace in actuator space spanned by the DM modes.

III. ADAPTIVE CONTROL

The adaptive control loop is enclosed in the dashed box in Figure 2. This control loop augments the classical AO loop to enhance wavefront prediction and correction, particularly for higher-order wavefront modes. The main component of this loop is the filter $L(z)$. The gains in this filter are updated adaptively. This adaptation may be either fully adaptive (i.e., at each time step) or quasi adaptive (i.e., periodically).

For identification of the filter gains, the problem is formulated as a feedforward disturbance-rejection problem with reference signal

$$r = G(z)u - E_1 y \quad (5)$$

and tuning signal

$$e = E_1 y, \quad (6)$$

as indicated in Figure 2. The transfer function $G(z)$ is an approximation to the transfer function from the control signal u to the tuning signal e with only the classical AO loop closed, and E_1 is a constant matrix. Thus, the input to the filter $L(z)$ is r , and the gains in $L(z)$ are identified to minimize the RMS value over time and space of e (equivalently, the RMS value over time of $\|e\|$).

In this paper, $E_1 = E_0$. The matrix E_1 will be different from E_0 if, for example, the adaptive loop is used for only some of the DM modes controlled by the classical AO loop. In this case, E_1 contains the rows of E_0 corresponding to the DM modes for which the adaptive loop is used.

With the hypothesis in (1), the condition (3) and the condition $E_1 = E_0$, the control channels represented by the columns of the matrix V are uncoupled in the classical AO

loop. The transfer function $G(z)$ then reduces to the following scalar transfer function for each channel:

$$G(z) = \frac{-K_1 z^d}{z^d - z^{d-1} + K_1}. \quad (7)$$

The modeling error between this transfer function and the true transfer function from u to e results from the error between (1) and the true mapping from the DM commands to the WFS vector. Extensive simulation results have demonstrated that the adaptive loop compensates for this modeling error.

The filter $L(z)$ in the adaptive control loop could be either FIR or IIR. While an IIR filter theoretically would produce optimal steady-state performance for stationary disturbance statistics, an FIR filter of sufficient order can approximate the steady-state performance of an IIR filter, and the convergence of the adaptive algorithm for an FIR filter is more robust with respect to modeling errors. In most adaptive optics problems to which the current methods have been applied, FIR filter orders greater than eight do not offer further performance improvement. Hence, an FIR filter is used in this paper. As the gains in the filter $L(z)$ are updated repeatedly, they converge to optimal constant gains when the disturbances have constant statistics.

The common form for an FIR filter of order n with input signal r and output signal u is

$$u = \sum_{k=1}^n A_k z^{k-1} r \quad (8)$$

where each A_k is a coefficient matrix with dimensions determined by the number of output channels and input channels. The adaptive controller here uses a lattice realization of the FIR filter $L(z)$, which is quite different from the realization in (8). The lattice realization is more complex than the realization in (8), but it has important advantages in terms of numerical stability and efficiency in RLS estimation of optimal filter gains for large orders and large numbers of channels. The FIR lattice filter used here is based on the multichannel lattice filter presented in [12], which derives numerical stability and efficiency from an orthogonalization of the data channels.

An important result follows from the fact that, under the condition (3), the control channels are uncoupled in the classical AO loop: The RLS problem for identifying the optimal filter $L(z)$ reduces to a set of independent RLS problems for the gains in the individual rows of $L(z)$. This makes the RLS problem at least tractable for real-time computation, although still challenging because of the large number of channels. The adaptive filtering problem to determine the optimal gains for $L(z)$ is still multichannel, so that the on-line algorithm for adaptively determining the filter gains must be numerically stable in the presence of many channels.

Even though the channels in the signals v , u , and e are uncoupled for the classical AO loop, all channels in the reference signal r feed into each channel of the adaptive control command u . Hence, the channels are coupled with the adaptive loop closed. Specifically, in predicting each channel of the error signal e , the adaptive filter uses the data from all

channels, so that the prediction is based on both spatial and temporal information.

IV. FIXED-GAIN FIR LOOP

When the statistics of the turbulence, platform jitter, and any other disturbances are stationary, the gains in the adaptive filter $L(z)$ in the adaptive control loop converge to constant values. Once these steady-state gains have been, the adaptive control loop is equivalent to a much simpler controller, in which the filter $L(z)$ is a fixed-gain FIR filter. This suggests an alternative, quasi-adaptive implementation of the FIR augmentation to the classical AO loop for applications where the statistics of the turbulence and other disturbances vary slowly or not at all during an engagement. In the quasi-adaptive implementation, the FIR gains can be estimated from a limited amount of wavefront-sensor data and then applied in the control loop. If necessary, the FIR gains can be updated periodically. Whether the FIR gains are identified only once or updated periodically, the quasi-adaptive implementation eliminates the significant real-time computational burden of updating the FIR gains in each sampling interval.

For estimation of fixed FIR gains, the classical AO loop and track loop are closed and a sequence of wavefront-sensor frames is collected and used for least-squares estimation of the FIR gains. For the simulation results in Section VI, the RLS lattice filter was used to identify the gains, but in principle, a batch least-squares method could be used.

There also are options for how the WFS data used in the identification is collected. This data was collected in two ways for results presented in Section VI. The most obvious is to collect a single sequence of consecutive WFS frames. For the simulation model used in this paper, 5000 WFS frames (one second's worth of data) has been sufficient for identification of very near optimal FIR gains. In the second method used for collecting WFS data for identification of the FIR gains, 1000 consecutive frames were saved from each of five simulations with five different random seeds for generating the turbulence phase screens, and these five sequences were conjoined to produce a single sequence of 5000 frames. Since the basic idea in identifying the FIR gains is to identify correlations between the wavefront sequence and backward shifts of itself, the number of independent sequences that can be conjoined is limited because the correlations will not hold across the boundary between two sequences. However, in the simulations presented here and numerous others, the FIR gains identified from five independent sequences of length 1000 each performed as well as the gains identified from a single sequence of 5000 frames in the control loop.

A final important point about identification of the FIR gains: the performance of the fixed-gain FIR loop must be evaluated by a simulation that uses a different random seed from any of those used to generate the WFS data for identification of the gains. This was the case for the results presented in Section VI.

V. FREQUENCY-WEIGHTED DM MODES

A. The Need for Frequency-weighted Orthogonal DM Modes for Adaptive Control

Orthogonal DM modes are essential for the adaptive control scheme discussed in Section III for two reasons: (1) so that $\|e\|$ is a physically meaningful least-squares objective function for identification of the adaptive filter gains; (2) well chosen modes permit the use of significantly fewer control channels, thus greatly reducing the real-time computational burden of the adaptive control loop.

Several methods for developing orthogonal deformable-mirror modes for use in adaptive optics with adaptive control have been introduced in [8], [9], [10]. These methods yielded useful modes, but they had certain undesirable features. The methods in [8], [9] require a gramian matrix for the actuator influence functions that usually is not available for real deformable mirrors, and the method in [10] tends to produce modes with mixed low and high spatial frequency content.

The DM modes in Figure 3 illustrate the main problem that the frequency-weighted modes introduced in this paper were derived to fix. Figure 3 shows the first six of 194 tilt-removed DM modes determined by a singular-value-decomposition (SVD) of the poke matrix for the simulation model in this paper. This is the method in [10] for computing orthogonal DM modes. While modes 3 and 4 are reasonably smooth, the other four mix low-frequency patterns with high-frequency content.

The frequency-weighted DM modes introduced in this paper eliminate mixing of low and high spatial frequencies. The method here produces a sequence of orthogonal DM modes that are ordered according to spatial frequency content so that the first modes in the sequence are very smooth and the dominant spatial frequencies increase with the mode number.

The basic method here requires only the actuator geometry. No information about the statistics of atmospheric turbulence is used. If there is any pre-imposed actuator slaving, the a matrix defining this slaving is required. If, as is common in applications, tilt-removed DM modes are desired, a set of tilt-removed basis vectors in actuator space is required. These initial vectors usually are computed using a poke matrix for the DM-WFS combination; they need not be orthogonal or frequency-weighted in any sense.

Low-pass spatial filtering has been used previously in classical AO loops to eliminate high-frequency noise from DM commands. Notably, low-pass filtering the reconstructed phase was shown in [14] to mitigate the effect of misregistration of actuator and sensor geometry. The way that the frequency-weighted DM modes are used here has the effect of first low-pass filtering the WFS vector and then generating DM commands with limited spatial-frequency bandwidth. The idea of frequency-weighted DM modes is new, although a relevant precedent is [9], where Zernike functions were approximated by linear combinations of actuator influence functions and the resulting DM shapes orthogonalized. Of course, generating DM modes by approximating Zernikes is not new, but for

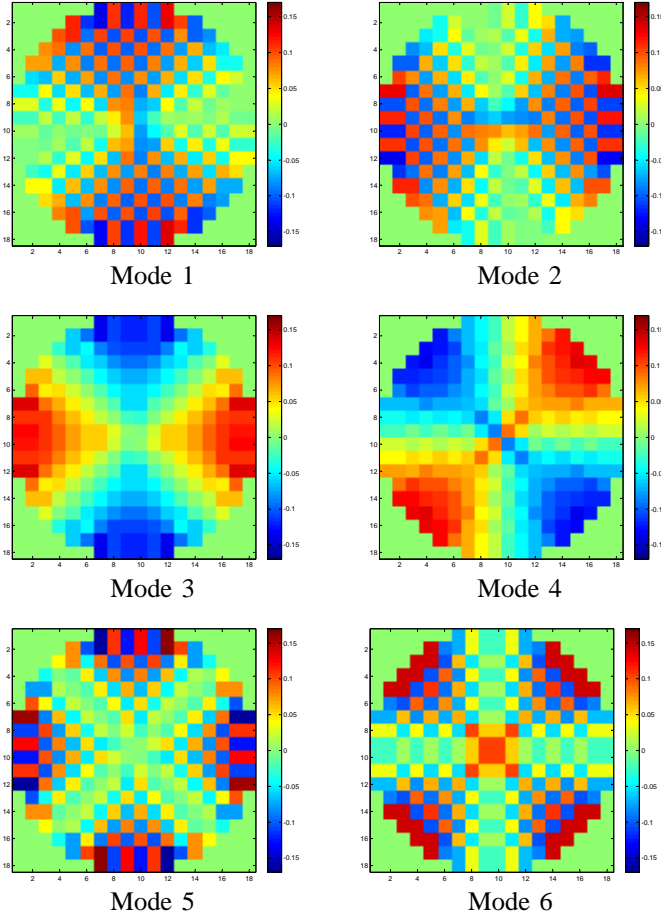


Fig. 3. Modes from SVD of poke matrix, first six of 194 modes.

finite numbers of actuators and most geometries the resulting DM modes are not orthogonal as needed for adaptive control in adaptive optics. The process of building the discrete approximations to Zernikes and then re-orthogonalizing as in [9] is tedious for complicated DM geometries, particularly with slaved actuators, and does not appear to be guaranteed to preserve separation of low and high frequencies.

B. Frequency-weighted Modes Orthogonal in Actuator Space

Let T be a matrix whose columns are a set of basis vectors in the space of master actuators (i.e., the actuators that can be commanded independently), and let S be the slaving matrix that maps the master actuators to all actuators. Thus, the columns of ST are a set of basis vectors in the space of all actuators. If there is no pre-imposed slaving, then S is the identity. Often in applications, the columns of T are constructed so that each column represents a DM shape with zero mean displacement and zero mean tilt. In this case, each of the final frequency-weighted modes will have zero mean displacement and zero mean tilt. Also in this case, the matrix T will not be square. If no such constraints are required, the T matrix can be the identity. In any case, the columns of T need not be orthogonal in any sense and need not have any type of frequency weighting.

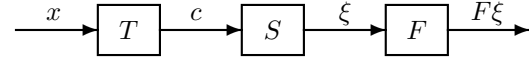


Fig. 4. Block diagram for the design of frequency-weighted DM modes.

The construction of frequency-weighted DM modes uses the series of transformations of DM commands illustrated in Figure 4. Any master-actuator command vector equal to a linear combination of the columns of T can be written as

$$c = Tx \quad (9)$$

where x is a coefficient vector. The slaving matrix S maps c to the vector ξ , which contains commands for all the actuators. Next, a low-pass filter F maps the command vector ξ to the vector $F\xi$. The problem of designing frequency-weighted DM modes now can be stated as the following:

Design Problem for DM Modes. *If T has m columns, determine a set of m unit vectors $\xi_i \in \text{range}(ST)$ such that*

- 1) ξ_1 maximizes $\|F\xi\|$ over all unit vectors $\xi \in \text{range}(ST)$;
- 2) for $1 < i \leq m$, ξ_i maximizes $\|F\xi\|$ over all unit vectors $\xi \in \text{range}(ST)$ that are orthogonal to all ξ_j , $1 \leq j < i$.

A set of vectors ξ_i that solve this problem can be constructed as the columns of the matrix

$$[\xi_1 \ \xi_2 \ \dots \ \xi_m] = STX \quad (10)$$

where X is the eigenvector matrix for the problem

$$(FST)^*(FST)X = (ST)^*(ST)XA^2 \quad (11)$$

with A^2 the diagonal matrix containing the eigenvalues λ_i^2 . Also,

$$\|F\xi_i\| = \mu_i \|\xi_i\| = \lambda_i, \quad i = 1, \dots, m, \quad (12)$$

The filter F can be represented either as a matrix that is multiplied by a vector ξ or as a two-dimensional array that is convolved with a two dimensional array into which a vector ξ is mapped. The latter representation probably will be generated directly in most applications.

In the space of master actuators, the frequency-weighted modes are represented by the m columns of the matrix

$$V = TX. \quad (13)$$

When the DM degrees of freedom represented by these modes are to be used for adaptive optics, then (9) becomes

$$c = Vv \quad (14)$$

where the m -vector v contains the modal commands. In most applications, only the first \tilde{m} DM modes ($\tilde{m} < m$) will be used for adaptive optics. In this case, only the first \tilde{m} columns of the matrix V are used in (9) and the command vector v has dimension \tilde{m} . Omitting the $m - \tilde{m}$ modes with highest spatial frequency produces low-pass spatial filtering in the AO loop.

C. Frequency-weighted Modes Orthogonal in Actuator Space and Sensor Space

The DM modes described in Section V-B usually are not orthogonal in sensor space. A set of frequency-weighted modes generated as in Section V-B can be made orthogonal in both actuator space and sensor space by the following procedure.

Let Γ be the poke matrix in (1), let S be the slaving matrix in Section V-B, and let V be the matrix whose \tilde{m} columns represent the frequency-weighted DM modes to be used for adaptive optics. Consider the vectors $\tilde{\xi}_i \in \text{range}(SV)$ defined by

$$[\tilde{\xi}_1 \ \tilde{\xi}_2 \ \dots \ \tilde{\xi}_{\tilde{m}}] = S\tilde{V} \quad (15)$$

where

$$\tilde{V} = V\tilde{X} \quad (16)$$

and \tilde{X} is the $\tilde{m} \times \tilde{m}$ eigenvector matrix for the problem

$$(\Gamma SV)^*(\Gamma SV)\tilde{X} = (SV)^*(SV)\tilde{X}\tilde{\Lambda}^2. \quad (17)$$

The vectors $\tilde{\xi}_i$ are mutually orthogonal in the space of all actuator commands and the vectors $\Gamma\tilde{\xi}_i$ are mutually orthogonal in sensor space. Also, $\text{range}(\tilde{V}) = \text{range}(V)$ in the space of master actuator commands and $\text{range}(S\tilde{V}) = \text{range}(SV)$ in the space of all actuator commands.

Figure 5 shows the geometry of the 256 actuators in the directed energy system used for the simulations in this paper. The 196 master actuators are represented by red circles, and the slaved actuators are represented by blue plus signs. The Hartmann wavefront sensor in this problem has 156 subapertures, so that the wavefront sensor vector y has dimension 312. Hence, the poke matrix Γ has dimensions 312×196 .

Figure 6 shows the eighth-order low-pass spatial filter F used to design the frequency-weighted modes. To obtain this filter, a one-dimensional linear-phase low-pass FIR filter of order $n_1 = 8$ and normalized cutoff frequency $\omega_1 = 0.5$ was mapped to a two-dimensional filter via the McClellan transformation [15]. The filter was produced by the MATLAB commands

$$F_1 = \text{fir1}(n_1, \omega_1), \quad F = \text{ftrans2}(F_1). \quad (18)$$

Different methods could be used for designing the two-dimensional filter F . For the DM geometry in this paper, the DM mode shapes did not change greatly with variations in n_1 and ω_1 .

After frequency-weighted modes were computed as in Section V-B, the first 40 modes were selected for use in the adaptive optics problem, and these modes were orthogonalized in sensor space according to (15)–(17). The 196×40 matrix \tilde{V} was used then for the matrix V in Figure 2.

Figure 7 shows examples from the 40 DM modes used in the simulations for this paper. Many of the frequency-weighted DM modes resemble Zernike functions. Similar DM shapes can be generated by evaluating Zernikes at actuator locations, but the resulting DM modes then must be orthogonalized because they only approximate continuous Zernikes on a circle.

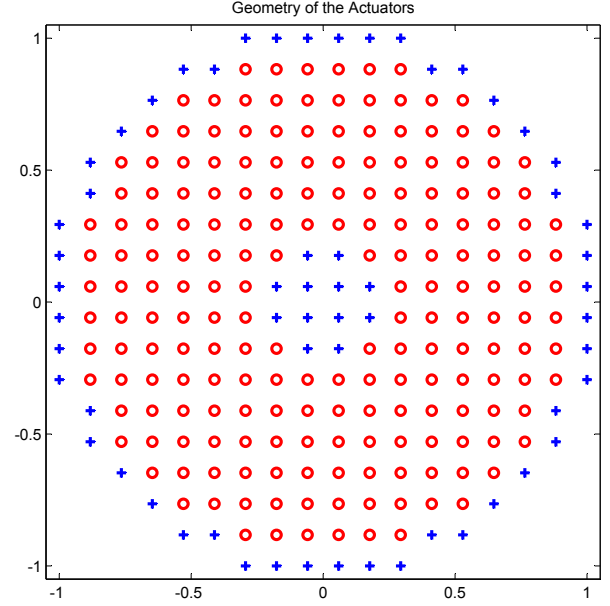


Fig. 5. DM actuator geometry: 196 master actuators (red \circ), 60 slaved actuators (blue $+$).

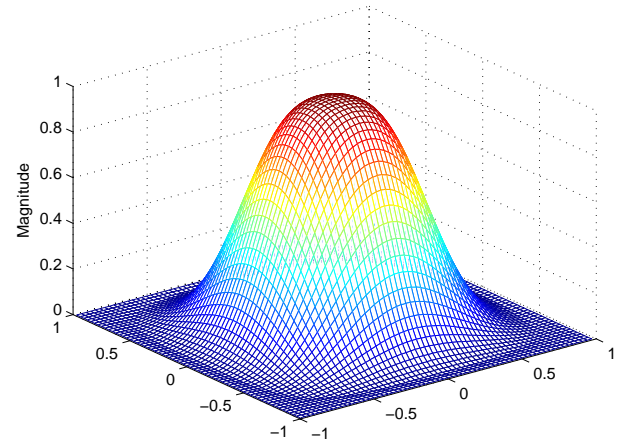


Fig. 6. Low-pass spatial filter used in design of DM modes.

This approach was used in [9], but it is tedious for complicated DM geometries with slaved and shadowed actuators, and the orthogonalization of the discrete approximations to Zernikes is not guaranteed to preserve separation of low and high frequencies.

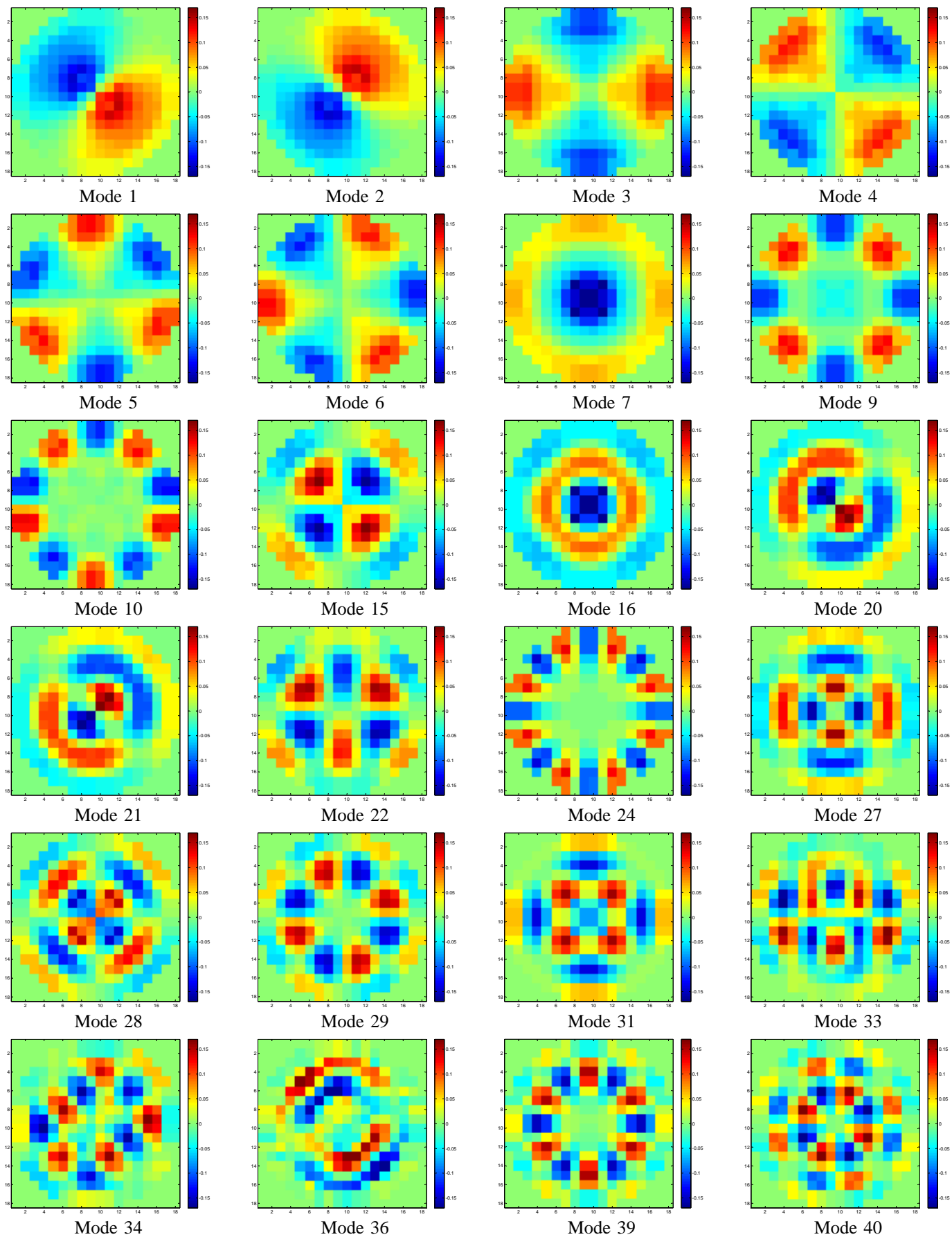


Fig. 7. Examples of the frequency-weighted DM modes used in simulations.

VI. SIMULATION RESULTS

The adaptive optics problem described in Section II was simulated with the control loops described in Sections II, III and IV. The most important parameters for the WaveTrain wave optics propagation model of the high energy laser (HEL) system are listed in Table I. For the simulation results presented here, the beacon for adaptive optics was a point source. Subsequent simulations have shown the adaptive control method presented here to be effective also in simulations with extended beacons.

TABLE I
PARAMETERS FOR WAVETRAIN WAVE OPTICS PROPAGATION (WOP)
MODEL OF HIGH ENERGY LASER SYSTEM

HEL path length	266700 m
HEL platform altitude	12200 m
Target altitude	29000 m
Platform velocity vector	(150 m/s, -150 m/s)
Target velocity vector	(1620 m/s, 0)
Wind velocity vector	(0, 0)
Turbulence strength	$2 \times \text{CLEAR I}^a$
Number of phase screens	16
Primary aperture	1.5 m
Pixel size on target	0.0468 m
Control and sensor frame rate	5000 Hz
<i>Wavelengths</i>	
High energy laser (HEL)	1.315 micron
Beacon illuminator (BILL)	1.064 micron
Track illuminator (TILL)	1.030 micron

^aCLEAR I is an optical turbulence model based on measurements of the atmosphere above the New Mexico desert. A detailed discussion of this model can be found in [16].

The performance of the standard AO and adaptive control loops was evaluated by their ability to concentrate HEL energy on the target. In the simulation, the energy distribution on the target was measured by a 100×100 -pixel image, which was recorded for each time step. This sequence was used to calculate the following approximate Strehl ratios:

- 1) The *Higher-order Strehl* is the average intensity over the four pixels nearest the centroid of each frame of the on-target HEL image (i.e., energy distribution).
- 2) The *Long-term Peak Strehl* is the maximum intensity over all pixels in an image formed by averaging frames 5001:7000 of the on-target HEL image.
- 3) The *Long-term Five-point Strehl* is the average intensity over the pixel where the Long-term Peak Strehl occurs and its four nearest neighbors.

Each of these Strehl criteria was normalized by the peak intensity of the on-target image in a simulation with zero turbulence, so that each Strehl is a ratio.

Figures 8 and 9 and Table II present results for simulations with $d = 1$ in Figure 2; i.e., a loop latency of one frame.

Figures 10 and 11 and Table III present results for simulations with $d = 2$. For the results in Figures 8, 9, 10 and 11, the 40 frequency-weighted modes described in Section V-C were used. (Some of these modes are shown in Figure 7.) Tables II and III list results for these 40 modes as well as corresponding results obtained with all 194 tilt-removed modes. Using 194 modes is equivalent to driving all master actuators independently and using a tilt-removed least-squares reconstructor. The long-term Strehl values listed in the tables under 40 modes were computed from the energy distributions shown in Figures 9 and 11 and corresponding distributions for the fixed-gain FIR implementation.

For the simulation results in this section, the order of the FIR filter was eight in both the adaptive loop and the fixed-gain FIR loop, and the integrator gains in Figure 2 were $K_1 = K_2 = 0.5$. Simulations with higher FIR orders did not show significant performance increases.

For the simulations here, the FIR filter $L(z)$ in the adaptive controller has m inputs and m outputs where m is the number of DM modes used. The number of scalar gains in the standard FIR realization in (8) is then nm^2 ; i.e., 12,800 gains for 40 DM modes and 301,088 gains for 194 modes. The lattice realization of the filter has approximately $4nm^2$ gains, but RLS estimation performed by the lattice filter is equivalent to estimating nm^2 independent gains.

In the plots in Figures 8 and 10, each point is the average of the higher-order Strehls for the 50 most recent frames of the on-target HEL energy distribution. This smoothing, which approximates the effect of a camera shutter speed of 100 Hz, filters some high-frequency temporal fluctuations in the energy distribution and makes the three time series plotted more readily distinguishable.

The adaptive control loop requires a learning period during which the adaptive control signal u is zero and the adaptive filter estimates optimal gains. In the simulations reported here, this learning period was 1000 frames, or 0.2 sec. As can be seen from Figures 8 and 10, the adaptive control loop is closed (i.e., u becomes nonzero) at the end of the learning period, and there is an immediate improvement in the on-target Strehl ratios, even though the gains in the adaptive filter have not converged to their optimal when the adaptive loop is closed initially. The gains converge to the optimal values between 4000 and 5000 frames (i.e., between 0.4 sec and 0.5 sec) when optimal steady-state performance is achieved.

As should be expected, all performance indices are lower with two loop delays than with one delay. Because the adaptive filter predicts the wavefront error, whereas the classical AO loop does not, it is not surprising that the improvement made by the adaptive control loop relative to the classical AO loop is greater for two delays than for one. It should be noted that, for each of the three performance indices, the value produced by the adaptive control loop for two delays is greater than the value produced by the classical AO loop for one delay (only slightly so for the long-term Strehls).

Figure 10 and Table III show results for the fixed-gain FIR loop discussed in Section IV, in addition to results for the

adaptive loop. For the fixed-gain FIR curve in Figure 10, the gains were identified from WFS data from a 5000-frame simulation with a single random seed. Table III also lists the performance indices for the fixed-gain FIR loop with the gains identified from data generated with five different random seeds, as discussed in Section IV. All the results in Figures 10 and 11 and Table III were generated with a single random seed that was different from any of the random seeds used to generate WFS data for identifying the fixed FIR gains. The optimal gains depend on the statistics of the turbulence, not on the particular realization.

The results show that the adaptive control loop performs slightly better than the fixed-gain FIR loop. The reason for this is that the adaptive loop can adapt to plant modeling errors whereas the fixed-gain FIR loop cannot. As mentioned in Section II, the model in (1) is only an approximation to the somewhat nonlinear relationship between the DM commands and the WFS vector. This linear model is used in identifying the gains for both the adaptive and fixed-gain loops, but the fixed-gain loop has no chance to correct for the modeling error because the gains are identified only once for the results here. If the fixed-gain FIR gains are re-identified periodically after the FIR loop is closed, then this loop also should correct for modeling error.

The adaptive loop performs essentially the same whether 40 DM modes or 194 modes are used, and likewise for the classical AO loop. This indicates that controlling the last 154 frequency-weighted modes is not important for improving the HEL on-target energy distribution. The fixed-gain FIR loop clearly performs better with only 40 DM modes, probably because the error between the true DM-WFS relationship and the model in (1) is greater in the high-frequency modes.

Using 40 modes instead of 194 yields a large reduction in the real-time computation requirement of the adaptive loop. Since the operation count for any of the best RLS algorithms, including the RLS lattice filter used here, is $O(m^2)$ where m is the number of channels, the real-time computation burden for 194 modes is more than 20 times that for 40 modes.

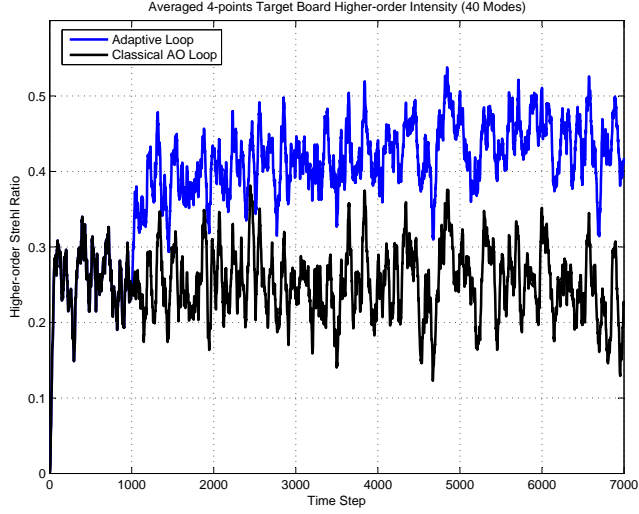


Fig. 8. Higher-order Strehls. Blue: adaptive control loop with 1000 learning steps; Black: classical AO and track loops only. One loop delay ($d = 1$).

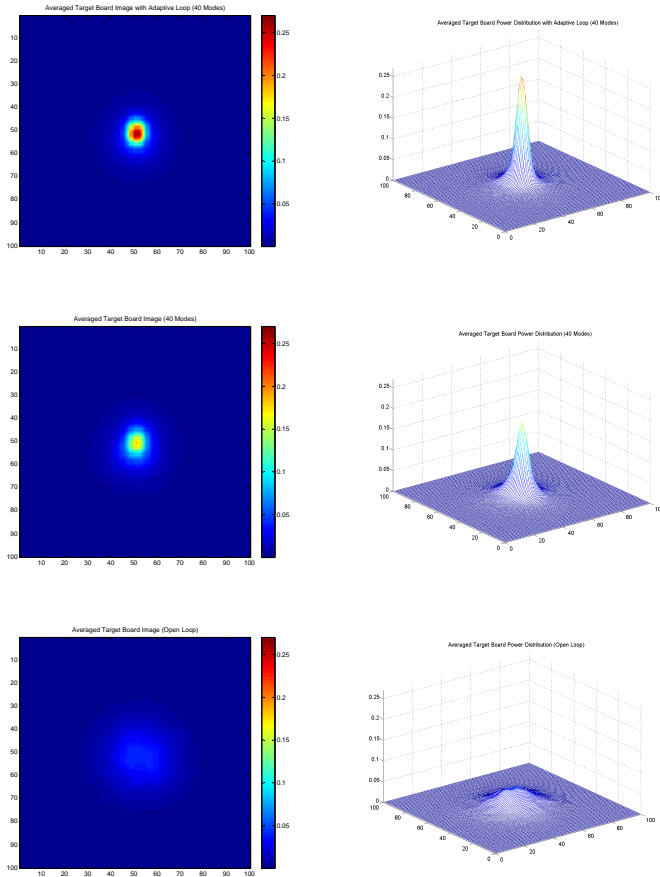


Fig. 9. Average on-target energy distribution for frames 5001:7000. Images (left) and mesh plots of intensity (right). Top: classical AO with adaptive loop; middle: classical AO and track loops only; bottom: open loop. One loop delay ($d = 1$).

TABLE II
PERFORMANCE CRITERIA FOR ONE LOOP DELAY ($d = 1$)
COMPUTED FOR FRAMES 5001:7000

Average Higher-order Strehls		
	194 Modes	40 Modes
Classical AO and Track Loops Only	0.2523	0.2469
Adaptive Control Loop	0.4201	0.4380
Open Loop	0.1139	

Long-term Peak Strehls		
	194 Modes	40 Modes
Classical AO and Track Loops Only	0.1799	0.1781
Adaptive Control Loop	0.2550	0.2615
Open Loop	0.0422	

Long-term Five-point Strehls		
	194 Modes	40 Modes
Classical AO and Track Loops Only	0.1743	0.1722
Adaptive Control Loop	0.2455	0.2419
Open Loop	0.0415	

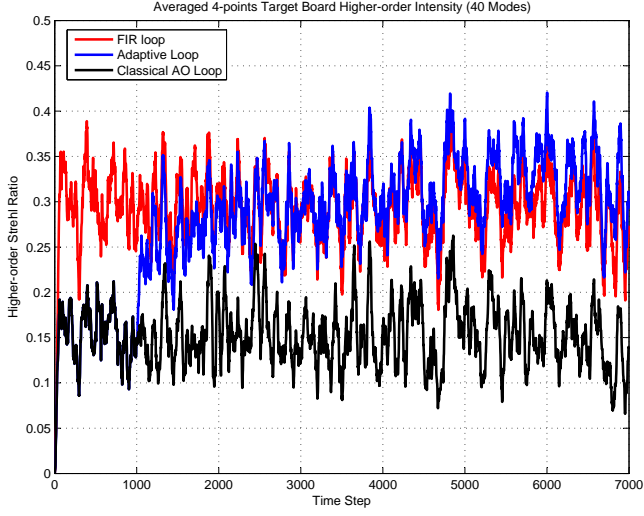


Fig. 10. Higher-order Strehls. Red: fixed-gain FIR loop; Blue: adaptive control loop with 1000 learning steps; Black: classical AO and track loops only. Two loop delays ($d = 2$).

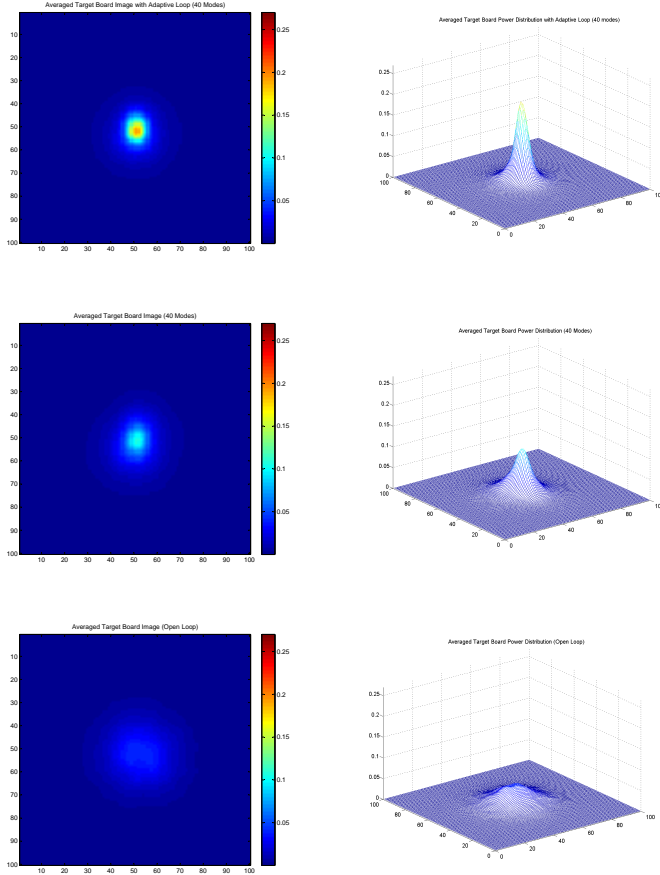


Fig. 11. Average on-target energy distribution for frames 5001:7000. Images (left) and mesh plots of intensity (right). Top: classical AO with adaptive loop; middle: classical AO and track loops only; bottom: open loop. Two loop delays ($d = 2$).

TABLE III
PERFORMANCE CRITERIA FOR TWO LOOP DELAYS ($d = 2$)
COMPUTED FOR FRAMES 5001:7000

Average Higher-order Strehls		
	194 Modes	40 Modes
Classical AO and Track Loops Only	0.1431	0.1480
Fixed-gain FIR Loop ID with one random seed	0.2451	0.2874
Fixed-gain FIR Loop ID with five random seeds	0.2490	0.2874
Adaptive Control Loop	0.3055	0.3230
Open Loop	0.1139	

Long-term Peak Strehls		
	194 Modes	40 Modes
Classical AO and Track Loops Only	0.1024	0.1071
Fixed-gain FIR Loop ID with one random seed	0.1515	0.1771
Fixed-gain FIR Loop ID with five random seeds	0.1547	0.1765
Adaptive Control Loop	0.1828	0.1934
Open Loop	0.0422	

Long-term Five-point Strehls		
	194 Modes	40 Modes
Classical AO and Track Loops Only	0.1004	0.1048
Fixed-gain FIR Loop ID with one random seed	0.1473	0.1664
Fixed-gain FIR Loop ID with five random seeds	0.1466	0.1662
Adaptive Control Loop	0.1736	0.1799
Open Loop	0.0415	

VII. VARYING THE GAIN IN THE CLASSICAL AO LOOP

This section describes how the performance of the classical AO loop and the performance of the adaptive control loop vary with the gain K_1 in Figure 2. The results here show why the gain $K_1 = 0.5$ was used for the simulations described in the previous sections of the paper, and the results here show how modeling errors associated with K_1 affect the performance of the adaptive loop.

The adaptive controller uses the transfer function $G(z)$ in (7) with the gain K_1 , but in some applications a more accurate representation of the true AO system will be

$$G_0(z) = \frac{-K_0 z^d}{z^d - z^{d-1} + K_0} \quad (19)$$

where K_0 is the product of the integrator gain and any unmodeled gains associated with the deformable mirror and wavefront sensor. Usually, $G_0(z)$ or any other linear transfer function at best approximates the true mapping from the adaptive control commands to the wavefront sensor measurements, due to nonlinearities not modeled in the control design. This is the case in the simulations for this paper, as discussed in Section II.

Figure 12 shows how the performance of the classical AO loop and that of the adaptive control loop vary with K_1 when $K_1 = K_0$. Figure 13 shows how the performance of the adaptive control loop varies with K_0 when K_1 has the fixed value 0.5. For all the results here, the value of the gain in the track loop in Figure 2 remained at $K_2 = 0.5$.

Table IV lists the ranges of gains for which simulations showed the AO system to be stable with the adaptive loop closed. If the linear model (1) were correct, the AO system with the adaptive loop would be stable whenever $G(z)$ is stable and $K_1 = K_0$; i.e.,

$$\begin{aligned} 0 < K_1 = K_0 < 2, & \quad \text{for } d = 1, \\ 0 < K_1 = K_0 < 1, & \quad \text{for } d = 2. \end{aligned} \quad (20)$$

The smaller stability intervals listed in Table IV result from nonlinearities in the WaveTrain model, which are not modeled for the adaptive controller.

The choice of $K_1 = 0.5$ for the results in Section VI was a compromise among the performance considerations represented in Figures 12–15. For two loop delays, $K_1 = 0.5$ is near optimal in terms of the higher-order Strehls, with the classical AO and feedback loops only and with the adaptive control loop. For one delay, Figure 12 shows that increasing K_1 to 1.0 increases the higher-order Strehl significantly, but Figure 14 shows that the larger K_1 also increases the sensitivity of the classical AO loop to high-frequency noise.

Figures 14 and 15 show the frequency responses of the sensitivity transfer function

$$S(z) = \frac{z^d - z^{d-1}}{z^d - z^{d-1} + K_1} \quad (21)$$

for one delay and two delays, respectively. If it is assumed that (1) gives the true mapping from the the DM command vector C and the disturbance (or noise) w to the wavefront

sensor vector y , and w and y are projected onto the images in sensor space of the DM modes, then the transfer function from each channel of w to the corresponding channel of y is $S(z)$. As illustrated by Figures 14 and 15, increasing the feedback gain increases the closed-loop bandwidth of the classical AO loop at the expense of amplifying the effects high-frequency wavefront error, sensor noise, and modeling error. With one delay, the sensitivity gain at the Nyquist frequency is $4/3 = 2.50$ dB for $K_1 = 0.5$ and $2.0 = 6.02$ dB for $K_1 = 1.0$. The increased high-frequency sensitivity would make $K_1 = 1.0$ less desirable in most applications.

Figures 12, 13 and 15 show overall lower performance and higher sensitivity for the case of two loop delays. The maximum sensitivity gain is already high for $K_1 = 0.5$, and $K_1 > 0.5$ produces higher sensitivity and decreasing higher-order Strehl beyond $K_1 = 0.6$. With the adaptive loop for two delays, both the higher-order Strehl and the sensitivity are somewhat better for $0.3 < K_1 < 0.4$, but only if $K_1 = K_0$ (i.e., there is no unmodeled gain in the system).

An important point illustrated by Figures 12 and 13 is that the adaptive controller yields Strehl ratios not achievable by the classical AO loop with any gain. This is not surprising, since unlike the adaptive loop, the classical AO loop has no prediction capability.

TABLE IV
STABILITY INTERVALS FOR ADAPTIVE CONTROL LOOP

Delay(s)	$K_1 = K_0$ (Fig. 12)	$K_1 = 0.5$ (Fig. 13)
$d = 1$	$0.00 < K_0 < 1.94$	$0.20 \leq K_0 < 1.10$
$d = 2$	$0.00 < K_0 \leq 0.80$	$0.27 \leq K_0 < 1.00$

VIII. CONCLUSIONS

The adaptive controller presented in this paper enhances control of higher-order wavefront errors. The adaptive loop predicts the wavefront to compensate for latency in the control loops, effectively extends the bandwidth of the classical AO loop, and adaptively compensates for plant modeling errors. The simulations of a directed energy system demonstrate the effectiveness of the adaptive control scheme in an application with extended turbulence, for both one and two-frame loop delays. Simulations also indicate that the fixed-gain implementation of the FIR loop performs nearly as well as the fully adaptive control loop if the turbulence statistics is stationary, and this implementation greatly reduces the real-time computation burden.

The method presented here for designing frequency-weighted orthogonal DM modes is important for the performance of the adaptive loop. These modes lead to the best tuning signal for the adaptive controller, and by allowing the use of a reduced number of control channels, the modes significantly reduce the computational burden of both the fully adaptive loop and the fixed-gain implementation.

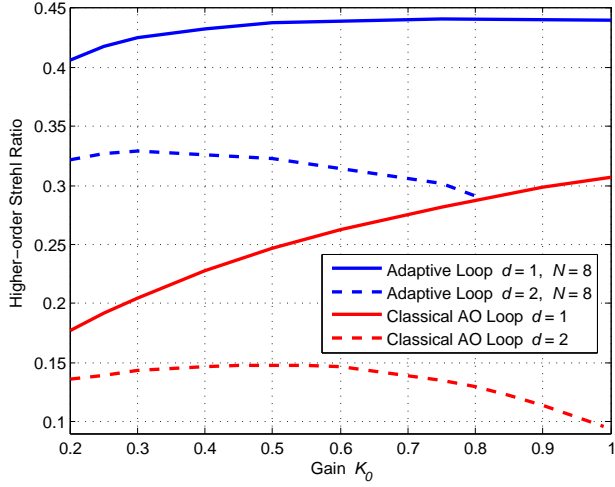


Fig. 12. Average higher-order Strehls (frames 5001:7000) for $K_1 = K_0$. Blue solid: standard AO and track loops with adaptive control, $d = 1$ (one loop delay); Blue dashed: standard AO and track loops with adaptive control, $d = 2$ (two delays); Red solid: standard AO and track loops only, $d = 1$; Red dashed: standard AO and track loops only, $d = 2$.

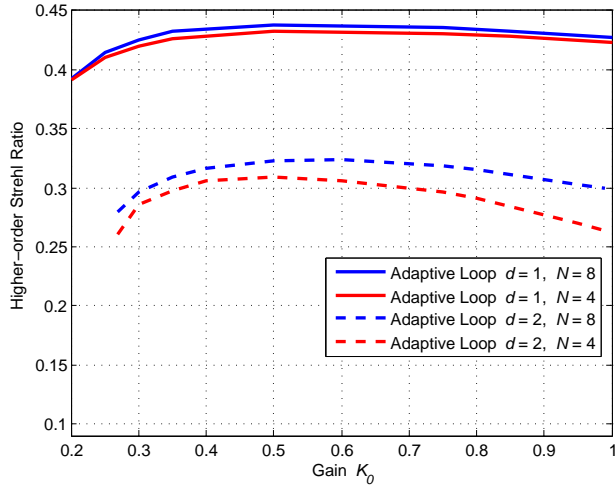


Fig. 13. Average higher-order Strehls (frames 5001:7000) for $K_1 = 0.5$. Standard AO and track loops with adaptive control for all cases. Blue solid: $d = 1$ (one loop delay), lattice-filter order $N = 8$; Red solid: $d = 1$, $N = 4$; Blue dashed: $d = 2$, $N = 8$; Red dashed: $d = 2$, $N = 4$.

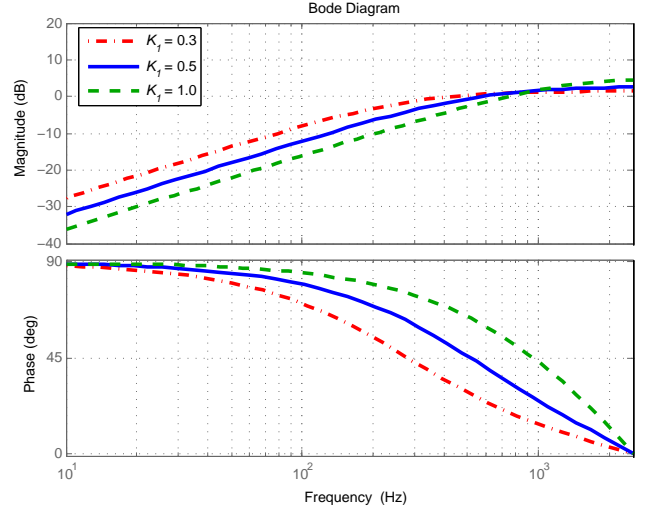


Fig. 14. Bode plots for sensitivity transfer function $S(z)$, $d = 1$. Solid curve: $K_1 = 0.5$; dashed curve: $K_1 = 1.0$.

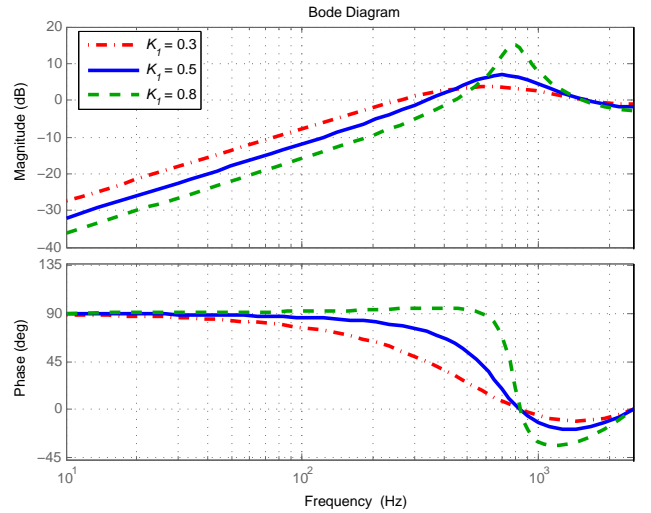


Fig. 15. Bode plots for sensitivity transfer function $S(z)$, $d = 2$. Solid curve: $K_1 = 0.5$; dashed curve: $K_1 = 0.8$.

REFERENCES

- [1] J. W. Hardy, "Adaptive optics," *Scientific American*, vol. 270, no. 6, pp. 60–65, 1994.
- [2] G. Rousset and J. C. Fontanella et al., "First diffraction limited astronomical images with adaptive optics," *Astron. and Astrophys.*, vol. 230, pp. L29–L32, 1990.
- [3] R. Q. Fugate and B. L. Ellerbroek et al., "Two generations of laser guide star adaptive optics experiments at the starfire optical range," *J. Opt. Soc. Am. A*, vol. 11, pp. 310–324, 1994.
- [4] B. L. Ellerbroek, C. Van Loan, N. P. Pitsianis, and R. J. Plemmons, "Optimizing closed-loop adaptive optics performance using multiple control bandwidths," *J. Opt. Soc. Am. A*, vol. 11, pp. 2871–2886, 1994.
- [5] M. Lloyd-Hart and P. McGuire, "Spatio-temporal prediction for adaptive optics wavefront reconstructors," in *Adaptive Optics*, M. Cullum, Ed., vol. ESO Conf. Proc. 54, European Southern Observatory, Garching, 1996, pp. 95–101.
- [6] B. L. Ellerbroek and T. A. Rhoadarmer, "Real-time adaptive optimization of wave-front reconstruction algorithms for closed-loop adaptive-optical systems," in *Adaptive Optical System Technologies*, ser. SPIE Proc., D. Bonaccini and R. Tyson, Eds., vol. 3353, 1998, pp. 1174–1183.
- [7] J. S. Gibson, C.-C. Chang, and B. L. Ellerbroek, "Adaptive optics: Wavefront reconstruction by adaptive filtering and control," in *38th IEEE Conference on Decision and Control*. Phoenix, Arizona: IEEE, December 1999.
- [8] —, "Adaptive optics: wavefront correction by use of adaptive filtering and control," *Applied Optics, Optical Technology and Biomedical Optics*, no. 16, pp. 2525–2538, June 2000.
- [9] C.-C. Chang and J. S. Gibson, "Parallel control loops based on spatial subband processing for adaptive optics," in *American Control Conference*. Chicago: IEEE, June 2000.
- [10] J. S. Gibson, C.-C. Chang, and Neil Chen, "Adaptive optics with a new modal decomposition of actuator and sensor spaces," in *American Control Conference*, Arlington, VA, June 2001.
- [11] Y.-T. Liu and J. S. Gibson, "Adaptive optics with adaptive filtering and control," in *American Control Conference*, Boston, MA, June 2004.
- [12] S.-B. Jiang and J. S. Gibson, "An unwindowed multichannel lattice filter with orthogonal channels," *IEEE Transactions on Signal Processing*, vol. 43, no. 12, pp. 2831–2842, December 1995.
- [13] *WaveTrain*, MZA Associates Corporation, Albuquerque, NM / Dayton, OH, www.mza.com.
- [14] Terry J. Brennan, "Stability margin loss due to wavefront sensor misregistration: amelioration with spatial filtering techniques," in *Proceedings of SPIE*, vol. 4376, 2001, pp. 88–98.
- [15] Jae S. Lim, *Two-Dimensional Signal and Image Processing*. Englewood Cliffs, NJ: Prentice Hall, 1990.
- [16] Robert R. Beland, "Propagation through atmospheric optical turbulence," in *The infrared & electro-optical systems handbook, Volume 2*, Frederick G. Smith, Ed. Bellingham, Washington USA: SPIE Optical Engineering Press, 1993, ch. 2, pp. 157–232.